Impacts of Model Fidelity on Trajectory Optimization for Autonomous Vehicles in Extreme Maneuvers

John K. Subosits [ORCID] and J. Christian Gerdes [ORCID]

Abstract—In this paper, we quantify the impacts of model fidelity on the effectiveness of trajectory optimization for autonomous vehicles when driving at the limits of friction through experiments with a full-size vehicle. Models ranging from a double-track model with lateral and longitudinal load transfer dynamics to a simple point-mass model are used in combination with direct numerical optimization to generate optimal trajectories subject to the limits imposed by each model. The effectiveness of each model for trajectory planning is evaluated by testing the trajectories on an automated vehicle across friction conditions ranging from ice to dry asphalt. Comparisons between the outright performance of the car and the car's ability to track the optimal trajectory are made across the various models. The tests reveal that the advantage of more complex models is less that they better predict the vehicle's behavior, but that they provide a more nuanced view of the vehicle's limits and guidance on the proper coordination of the various actuators on the vehicle in order to make most efficient use of the available tire friction.

Index Terms—Autonomous vehicles, trajectory optimization, vehicle dynamics.

I. INTRODUCTION

THE development of increasingly capable autonomous vehicles and improvements in computer hardware and software for numerical optimization have cast optimal control of automobiles into the limelight. While trajectory optimization was once primarily interesting from an academic perspective [1], the ability to solve numerical optimal control problems rapidly has led to an explosion of optimal trajectory planning and model predictive control (MPC) schemes for autonomous vehicles. MPC has been used to achieve a level of vehicle control approaching that of a human being in situations ranging from highway driving and lane changing, to parking, to emergency obstacle avoidance, to minimum time maneuvering [2]–[5]. Emergency obstacle avoidance and minimum time maneuvering differ from the other tasks in that they require operation at the vehicle's friction limits, albeit relatively briefly in the case of obstacle avoidance. This commonality means that insights from one field may be applied to the other and to any situation requiring operation at the limits.

A. Related Work

Studies of minimum time maneuvering and the adjacent problem of racing line optimization for motorsport have used a wide variety of models. Point-mass models which capture the translational, but not the rotational, dynamics of the vehicle have been used with success [6]–[8]. Because of their simplicity, these models are also widely used for online trajectory generation [9]–[12]. Single-track vehicle models do capture the freedom of a vehicle to rotate independently of its velocity vector [13], [14]. These models have also proven popular for examining how the road surface condition affects the optimal trajectory [15]–[17] and as the simplest model which captures the three fundamental degrees of freedom of an automobile, for MPC [2], [4], [5], [18]. Capturing this additional degree of freedom is important for vehicle yaw stabilization, that is, preventing the directions of the vehicle heading and velocity vectors from diverging. However, single-track models use a single tire to approximate the forces generated by an axle meaning that they fail to capture yaw moments from different drive and brake forces across an axle. To capture these effects, a double-track model, such as those used in [19]–[21], is required.

However, relatively few comparisons have been made of the effectiveness of the various types of models used. Notable exceptions are the work of Berntorp *et al.* which found, with one major exception, that little high level variation is seen in optimal trajectories generated with single-track and double-track models [22]. Gottman *et al.* compare point-mass and single-track models and highlight the importance of longitudinal load transfer [23]. This study expanded on the earlier finding of Liu *et al.* that longitudinal load transfer was a critical effect in the particular case of constant-speed obstacle avoidance for autonomous trucks [24]. However, the sensitivity of a real vehicle to the differences in optimal control inputs generated with the various models remains untested. Comparisons to real data have been limited to evaluation of models for vehicle state estimation [25]–[27]. However these studies are unable to provide guidance on the selection of a model of appropriate fidelity for optimal control.

While the significance of model fidelity for trajectory generation remains an open question, the more accurate description of yawing moments enabled by double-track models has proven critical to the design and development of stability control systems. Electronic Stability Control (ESC) systems control understeer and oversteer of the vehicle by braking individual wheels and occasionally reducing engine output [28], [29], and their widespread adoption has led to significant reductions in the number of road fatalities [30]. In addition to enhancing the

stability properties of the vehicle, torque vectoring across an axle has been shown to increase the achievable linear acceleration of a vehicle. Sawase *et al.* found that torque vectoring differentials have a significant effect on the vehicle's dynamic limit while Jonasson *et al.* found a similar advantage for individual electric motors at each wheel [31], [32]. More recent work by de Castro *et al.* and Smith demonstrated that controlling drive and brake torques at each of the four wheels through independent electric motors reduces the time needed to complete a corner at the limit of tire adhesion [33], [34].

The ability to divide torque across each axle is useful, but conventional automobiles lack the complex torque vectoring differential or independent motors required to do this arbitrarily. However, production automobiles do have a limited capability to do this through individual wheel braking, as in ESC, and possibly a limited slip differential (LSD) [35]. The limited capability of these systems make them more difficult to model and use for control. To model the true behavior of a vehicle equipped with an LSD, Limebeer and Perontoni take the numerically expedient approach of approximating it as a viscous friction coupling [36] while Tremlett *et al.* use a more complex empirical model for its behavior [37]. Both approaches show that a passive LSD can expand the steady-state operating regime of a vehicle and reduce lap times. Tremlett *et al.* carried this analysis farther by simultaneously optimizing the driver inputs and differential control strategy for a rear wheel drive race car with a controllable LSD performing a double lane change maneuver in [38]. However, the question of optimal coordination between individual wheel braking, as used in ESC, and an electronically controlled limited slip differential has not been addressed despite the fact that this is a common configuration for production automobiles.

B. Contributions

The contributions of this paper are threefold. First, it presents a model and an optimal control approach for coordinating the usage of four wheel independent brake-by-wire and an electronically-controlled limited slip differential. Second, while a double-track model is required to capture the effects of such a control scheme, we demonstrate that the choice of model fidelity does not have a major effect on the optimal racing line or actual lap time. Third, experimental results from a variety of surface conditions with varying friction coefficients are presented to support the theoretical results. This paper begins with an introduction of the models of varying complexity used within this paper. A description of the optimal control problem follows. Finally, the solutions for each of the models are compared to demonstrate the nuances of model choice and experimental data are presented to support the assessment of the suitability of each model for trajectory generation.

II. MODEL DERIVATION

Here we describe the models used to express the vehicle's dynamics. We first present the double-track and explain the modeling choices made before introducing the simplifications needed to obtain the single-track and point-mass models.
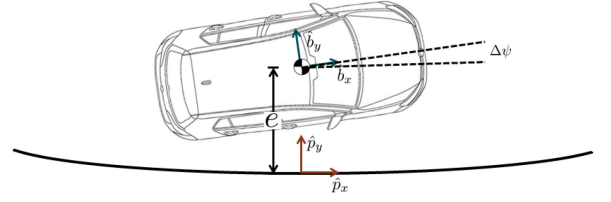

Fig. 1. Vehicle position and reference frames.

A. Kinematics of the Car and the Track

A reference path and an associated curvilinear coordinate system are used to describe the position of the vehicle. This reference path follows the three-dimensional surface of the road which allows us to account for the effects of topography on the vehicle. The following orthogonal unit vectors $\hat{p}_x$, tangent to and directed along the three dimensional path, $\hat{p}_y$, in the plane of the road surface and directed laterally towards the left edge, and $\hat{p}_z$, locally normal to the road surface and directed upwards, define a reference frame at a given distance s along the path. The path frame is obtained from an earth-fixed inertial one by successive rotations of ψ (yaw), θ (pitch), and ϕ (roll), and its origin is located at the point on the path closest to the center of mass of the vehicle. An additional reference frame is fixed to the vehicle with unit vectors $\hat{b}_x$ directed out the front of the car, $\hat{b}_y$ directed laterally out the left side, and $\hat{b}_z$ vertically. The body frame orientation differs from that of the path from by an additional rotation of $\Delta\psi$ about $\hat{p}_z$. The origin of this frame is fixed to the center of mass of the car and is displaced by $e\,\hat{p}_y$ from the origin of the path frame as illustrated in Fig. 1

We denote derivatives of x with respect to time t and distance along the path s as $\dot{x}$ and x', respectively. We also introduce $i = \phi' - \psi'\sin\theta$, the local twisting of the road surface, $j = \theta'\cos\phi + \psi'\sin\phi\cos\theta$, the component of the path's total curvature in the plane of the road, and $k = \psi'\cos\theta\cos\phi - \theta'\sin\phi$, the component of the curvature of the path aligned with the normal to the road surface. The angular velocity of the path frame relative to the inertial one is given by

$$^{N}\vec{\omega}^{P} = \dot{s}(i\,\hat{p}_x + j\,\hat{p}_y + k\,\hat{p}_z) \tag{1}$$

where $\dot{s}$ is the vehicle's rate of progress along the path.

B. Vehicle Model

We model the vehicle as a single rigid body with three degrees of freedom. As illustrated in Fig. 2, the longitudinal component of the vehicle's velocity is given by u_x, the lateral component by u_y, and the yaw rate by r. The vehicle is assumed to always move parallel to and remain aligned with the surface of the road which allows the roll rate p, the pitch rate q, and vertical velocity u_z to be obtained directly from kinematics. In sum, the velocity of the vehicle's center of mass is given by

$$^{N}\vec{v}^{cg} = u_x\,\hat{b}_x + u_y\,\hat{b}_y + u_z\,\hat{b}_z \tag{2}$$

and the vehicle's angular velocity is given by

$$^{N}\vec{\omega}^{B} = p\,\hat{b}_x + q\,\hat{b}_y + r\,\hat{b}_z. \tag{3}$$
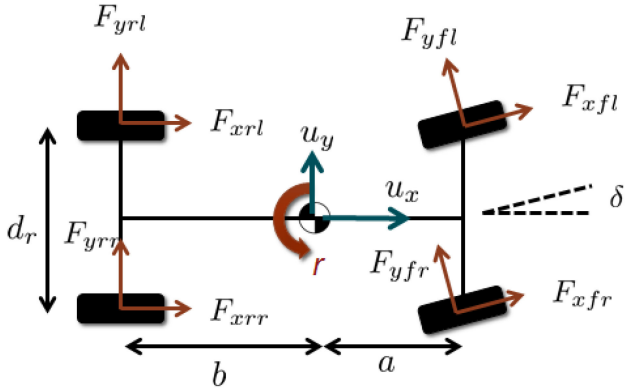
Fig. 2. Vehicle states and force vectors.

The vehicle has mass m and principle components of inertia given by I_{xx}, I_{yy}, and I_{zz}. Assuming left-right symmetry of the vehicle, $I_{xy} = I_{yz} = 0$. I_{xz} is neglected in this work since it is typically small [39]. The local gravitational acceleration is expressed as $\vec{g} = g_x \, \hat{b}_x + g_y \, \hat{b}_y + g_z \, \hat{b}_z$ and is obtained by applying a rotation from the inertial frame. The equations of motion for the double-track model are given by

$$\dot{u}_y = \frac{F_{yf} \cos \delta + F_{yr} + F_{xf} \sin \delta}{m} - ru_x + pu_z + g_y, \quad (4)$$

$$\dot{r} = \frac{a(F_{yf} \cos \delta + F_{xf} \sin \delta) - bF_{yr}}{I_{zz}}$$
$$+ \frac{\frac{d_r}{2}(F_{xrr} - F_{xrl}) + \frac{d_f}{2}(F_{xfr} - F_{xfl}) \cos \delta}{I_{zz}}$$
$$+ \frac{(F_{yfl} - F_{yfr}) \sin \delta)}{I_{zz}} + \frac{(I_{xx} - I_{yy})pq}{I_{zz}}, \quad (5)$$

$$\dot{u}_x = \frac{F_{xf} \cos \delta + F_{xr} - F_{yf} \sin \delta - F_{drag}}{m} + ru_y$$
$$- qu_z + g_x, \quad (6)$$

$$\dot{\Delta\psi} = r - \dot{s}k, \quad (7)$$

where

$$\dot{s} = \frac{u_x \cos \Delta\psi - u_y \sin \Delta\psi}{1 - ke}, \quad (8)$$

and

$$\dot{e} = u_x \sin \Delta\psi + u_y \cos \Delta\psi. \quad (9)$$

The shorthand $F_{xf} = F_{xfl} + F_{xfr}, F_{xr} = F_{xrl} + F_{xrr}, F_{yf} = F_{yfl} + F_{yfr}, \; F_{yr} = F_{yrl} + F_{yrr}, \; F_{zf} = F_{zfl} + F_{zfr},$ and $F_{zr} = F_{zrl} + F_{zrr}$ has been introduced for compactness.

The suspension dynamics of an automobile are complex. Dampers or shock absorbers are nonlinear in that their damping coefficients vary with both the speed and direction of motion. Different springs and dampers are used on each axle of a vehicle. These facts make it difficult to characterize the suspension accurately without specialized equipment. Due to this difficulty, load transfer in this work is modeled as a first order system, which asymptotically approaches steady state similar to the approaches used in [16] and [37]. In the literature, this approach, more complex linearized second order models, and simpler steady state constraints have all been used for vehicular trajectory optimization. In the model used here, lateral and longitudinal load transfer are captured by two variables, $\Delta F_{z, lat}$ and $\Delta F_{z, long}$ respectively. These variables effectively serve as proxies for roll and pitch of the chassis. The derivatives of the load transfer variables are given by

$$\dot{\Delta F}_{z, long} = -K_{long} \left(\Delta F_{z, long} + \frac{pr(I_{zz} - I_{xx})}{l} \right.$$
$$\left. - \frac{h(F_{xf} \cos \delta + F_{xr} - F_{yf} \sin \delta) + I_{yy}\dot{q}}{l} \right) \quad (10)$$

$$\dot{\Delta F}_{z, lat} = -K_{lat} \left(\Delta F_{z, lat} + \frac{qr(I_{zz} - I_{yy})}{d} \right.$$
$$\left. - \frac{h(F_{yf} \cos \delta + F_{yr} + F_{xf} \sin \delta) - I_{xx}\dot{p}}{d} \right) \quad (11)$$

where K_{lat} and K_{long} are constants chosen to approximate the dynamics of the suspension. Note that the required angular accelerations can be computed from track geometry and other states under the assumption that the vehicle remains aligned with the road surface. While not strictly necessary for trajectory optimization, incorporating even simple load transfer dynamics is advantageous for simulation and parameter fitting since modeled tire normal loads are always available directly as input to a tire model.

Typically, the rotational speed of the wheels are also needed to compute the longitudinal slip input to the tire model. An alternative approach used here is to assume that the wheel speeds remain in equilibrium and use a tire model which takes applied torque or, equivalently, the force required to balance it at the contact patch as an input. This is a reasonable simplification since the dynamics of each wheel are much faster than those of the vehicle as a whole due to the small rotational inertia and high longitudinal stiffness of the tire. Small time steps are needed to resolve these dynamics accurately, making any optimal control problem expensive to solve. Attempts to glean additional fidelity though the incorporation of wheel speeds must contend with the fact that in practice wheel speeds are heavily influenced by irregularities in the road surface and the operation of black box systems such as the ABS unit.

C. Tire Normal Loads

The normal load on a given tire determines the maximum force that that tire can generate through friction. Summing the forces normal to the road surface gives

$$F_z = m(-g_z + \dot{u}_z + pu_y - qu_x). \quad (12)$$

where $\dot{u}_z = \dot{e}\dot{s}i + e\dot{s}^2 i' + e\ddot{s}i$. Once the sum of the tires' normal loads has been computed, the load on each tire can be computed

as follows.

$$F_{zfl} = \frac{\frac{b}{L}F_z - \Delta F_{z,\,long}}{2} - \gamma \Delta F_{z,\,lat} \qquad (13)$$

$$F_{zfr} = \frac{\frac{b}{L}F_z - \Delta F_{z,\,long}}{2} + \gamma \Delta F_{z,\,lat} \qquad (14)$$

$$F_{zrl} = \frac{\frac{a}{L}F_z + \Delta F_{z,\,long}}{2} - (1-\gamma)\Delta F_{z,\,lat} \qquad (15)$$

$$F_{zrr} = \frac{\frac{a}{L}F_z + \Delta F_{z,\,long}}{2} + (1-\gamma)\Delta F_{z,\,lat} \qquad (16)$$

where the parameter γ denotes the fraction of lateral load transfer borne by the front axle. This parameter is of primary importance in determining the tendency of the vehicle to understeer or oversteer at the limit.

D. Tire Model

The tire model used with the double-track model here is a variant of the well known Fiala brush model [40], but it has been extended to better model the effects of normal load and longitudinal force on the parameters [41]. In its simplest form, the brush model needs only two parameters, a cornering stiffness C_α and a friction coefficient μ, to relate a slip angle, the difference between the orientation and direction of travel of a tire, to lateral force. However, in actuality, these parameters are not constants, but vary with normal load and longitudinal force [41], [42]. Capturing this dependence is necessary if a single tire model is to be used to describe the behavior of a vehicle with four identical tires.

As modeled here, a tire's maximum available lateral force is determined by the friction circle,

$$F_{y,\,max} = \sqrt{(\mu(F_z)F_z)^2 - F_x} \qquad (17)$$

and is generated at the slip angle at which which the tire just begins to slide

$$\alpha_{slide} = \frac{3F_{y,\,max}}{C_\alpha(F_z,\,F_x)}. \qquad (18)$$

The friction coefficient of the tire decreases linearly with increasing normal load,

$$\mu(F_z) = \mu_0 + \mu_{df_z}\left(\frac{F_z - F_{z0}}{F_{z0}}\right) \qquad (19)$$

where $\mu_{df_z} < 0$ is the sensitivity of the friction coefficient to normal load. This relationship permits the modeling of the vehicle's oversteering or understeering behavior at the friction limits. The cornering stiffness is also modified by both the longitudinal and normal force,

$$C_\alpha(F_z,\,F_x) = \frac{1}{2}(\mu F_z - F_x)$$
$$+ \left(1 - \left(\frac{|F_x|}{\mu F_z}\right)^n\right)^{1/n}\left(C_\alpha(F_z) - \frac{1}{2}\mu F_z\right) \qquad (20)$$
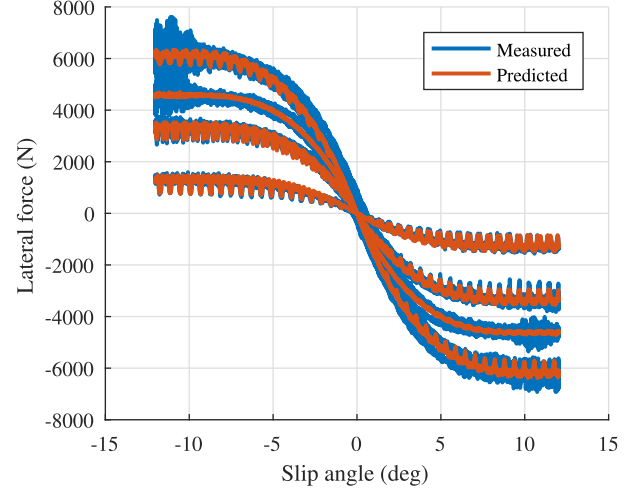

Fig. 3. Lateral force varies primarily with slip angle and normal force as seen in the distinct curves for normal loads of 1150, 3100, 4500, and 6200 Newtons exhaustively combined with inclination angles of -3, 0, and 3 degrees. Oscillations in the measured normal force cause the oscillations in predicted force which closely match the observed oscillations in measured lateral force.

where

$$C_\alpha(F_z) = c_1 F_{z0} \sin\left(2\arctan\left(\frac{F_z}{c_2 F_{z0}}\right)\right). \qquad (21)$$

The effect of longitudinal force on cornering stiffness serves as a proxy for the coupled slip behavior of the tire. When a larger fraction of the tire's friction potential is used for longitudinal force, a larger slip angle is needed to produce a given lateral force. Finally, the generated lateral force is given by the piecewise function

$$F_y(\alpha) = \begin{cases} -C_\alpha \tan\alpha \ldots \\ \quad + \dfrac{C_\alpha^2}{3F_{y,\,max}}\tan\alpha|\tan\alpha| \ldots \\ \quad - \dfrac{C_\alpha^3}{27F_{y,\,max}^2}\tan\alpha^3, & |\alpha| \leq \alpha_{slide} \\[2mm] -F_{y,\,max}\,\mathrm{sign}\,\alpha, & |\alpha| > \alpha_{slide} \end{cases} \qquad (22)$$

where the explicit dependence of the cornering stiffness on the longitudinal and normal forces has been dropped for compactness. We believe that this model captures the important physical effects without introducing an excessive number of parameters.

To illustrate the phenomena described above, we use the model to fit tire tester data for a tire of similar size and construction as those used on the test vehicle. Pure lateral slip behavior is shown in Fig. 3 for a variety of normal loads and inclination angles. The major changes in cornering stiffness and peak lateral force are well captured by the model despite the fact that the effects of inclination angle are not included. The inclination angle varies over a range of 8 degrees during the test, a larger range than will be seen on the vehicle. As illustrated by Fig. 4, demanding significant longitudinal force from the tire has a pronounced effect on the lateral force generated even at a small
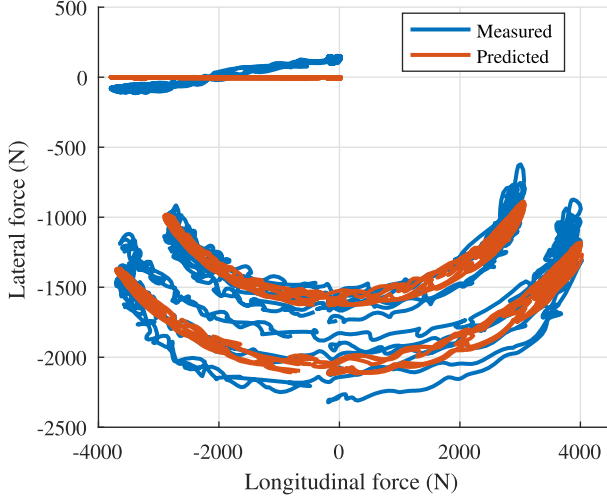
Fig. 4. Effect of longitudinal force on cornering stiffness for normal loads varying about mean values of 2600 and 3600 Newtons. As the inclination angle varies between -3, 0, and 3 degrees, the generated force changes. However on the vehicle, this effect cancels out between the left and right tires on the vehicle.

slip angle of 2 degrees. For this data set, a value of $n = 2.16$ was used. Clearly, cornering stiffness is highly dependent to both the applied normal and longitudinal forces

E. Differential Model

The last piece of modeling to consider is the effect of the electronically-controlled limited slip differential on the torque distribution between the two wheels. We consider a front wheel drive vehicle in this work, but the same considerations apply to a rear or all-wheel drive vehicle. When the differential is open, the tires are free to rotate independently and the engine torque applied to each is the same. The tire forces with the differential fully open are given by

$$F_{xfl,open} = \frac{F_{engine}}{2} + F_{xfl, \, brake} \qquad (23)$$

$$F_{xfr,open} = \frac{F_{engine}}{2} + F_{xfr, \, brake}. \qquad (24)$$

Conversely, when the limited slip differential is fully engaged, the wheels are forced to rotate at the same speed.

Since the limited slip differential relies on friction to operate, it cannot be used to distribute torque arbitrarily but only to apply more (positive) torque to the more slowly rotating wheel. When the differential is engaged, a model is needed to determine the longitudinal forces generated by each tire. Beginning with a simple linear model for the tire longitudinal forces, we have

$$F_x = C_x \kappa = c_8 F_z \kappa \qquad (25)$$

where C_x is the tire's longitudinal stiffness which is modeled as a linear function of normal load. A given tire's longitudinal slip, κ is give by

$$\kappa = \frac{\omega r_e - v_x}{v_x} \qquad (26)$$

where r_e is the tire's effective radius, v_x is the component of its translational velocity normal to its axis, and ω is its angular velocity. When the front differential is locked, $\omega_{fl} = \omega_{fr} = \omega$. With the differential locked, the longitudinal slip of each of the front wheels is given by

$$\kappa_{fr} = \frac{\omega r_e}{v_{xfr}} - 1 \text{ and } \kappa_{fl} = \frac{\omega r_e}{v_{xfl}} - 1 \qquad (27)$$

Inserting these quantities into (25) for the left and right wheels and rearranging to eliminate ωr_e gives

$$\left(\frac{F_{xfl}}{c_8 F_z} + 1 \right) v_{xfl} = \left(\frac{F_{xfr}}{c_8 F_z r} + 1 \right) v_{xfr} \qquad (28)$$

Eliminating F_{xfl} and F_{xfr} in turn and rearranging gives the following expressions for the longitudinal forces at each of the two front wheels when the differential is locked.

$$F_{xfl, \, locked} = \frac{F_{zfl} F_{xf} v_{xfr} + d_f c_8 r F_{zfl} F_{zfr}}{F_{zfr} v_{xfl} + F_{zfl} v_{xfr}} \qquad (29)$$

$$F_{xfr, \, locked} = \frac{F_{zfr} F_{xf} v_{xfl} - d_f c_8 r F_{zfl} F_{zfr}}{F_{zfr} v_{xfl} + F_{zfl} v_{xfr}} \qquad (30)$$

We define a control input $u_{diff} \in [0, 1]$ to describe the degree of locking in the differential so that the longitudinal force required of the front left tire is given by

$$F_{xfl} = (1 - u_{diff}) F_{xfl, \, open} + u_{diff} F_{xfl, \, locked}$$

with an analogous expression for the front right tire. These expressions quantify the physically achievable longitudinal force distributions.

This novel model for the effect of the differential on the vehicle's motion not only allows the removal of the wheel speed dynamics making the optimal control problem faster to solve but also makes the model easier to interpret and understand. For example, when driving straight ahead with equal loads on the two tires, locking the differential has no effect. At small yaw rates, $r \approx 0$, the difference in front wheel velocity in small, and the total normal force is distributed almost exactly according to the normal loads on each tire allowing efficient use of the available friction for acceleration. However, when the total longitudinal force is small, the outside wheel has a more negative force resisting the vehicle's turning. Finally, if the differential were to be engaged while braking, the magnitude of brake force on the outside tire would be increased. When there is significant lateral load transfer, the differential can be used to promote rotation of the vehicle when accelerating and resist it while braking. Mitigating the natural tendency of a front wheel drive vehicle to understeer and oversteer in these situations expands the performance envelope of the vehicle.

F. Single-Track and Point-Mass Models

A few changes are required to simplify the double-track model to a single-track model. As can be seen from (4)–(6), the only difference between the dynamics of the double-track and single-track models is that the single-track model does not include the second fractional term in (5) since $d_f = d_r = 0$ for the single-track model. Since the two tires at each axle are combined into

one, the lateral load transfer state $\Delta F_{z,\,lat}$ is removed. Without modeling lateral load transfer, normal load sensitivity cannot be used to capture the axles' differing behavior, so different parameters are used to model the lumped front and rear tires. Cornering stiffness and friction coefficients are made constant to match single-track models used elsewhere in the literature and to avoid introducing an excessive number of parameters to be estimated. Finally, since lateral differences in longitudinal force across an axle are no longer modeled, the four individual brake inputs are halved to one for each axle, and differential engagement is removed as a control input.

The same reduction in control inputs can also be applied to the double-track model to assess whether differences in performance between the models are attributable to model fidelity or the additional control flexibility afforded by the double-track model. This constrained double-track model operates identically to the double-track model described earlier, but lacks the ability to divide torque across an axle through differential braking or locking the differential. Effectively, the differential is constrained to remain open and the brakes to have the same pressure across each axle. Comparing this model and its more accurate dynamics and view of the limits to the other three helps to separate the effects of model fidelity and additional control inputs on tracking and racing performance.

The point-mass model used in this work is an even greater simplification in that it removes yaw dynamics from the vehicle model entirely. Instead, it is assumed that the tires can be used to generate forces directly, bounded by friction, removing the need for slip angles and a tire model. Accordingly, the equations of motion can be simplified by setting the steering angle $\delta = 0$. From this simplification and the steady state assumption that $u_y = \dot{u}_y = 0$, (4) simplifies to

$$ r u_x = \frac{F_y}{m} + p u_z + g_y. \tag{31} $$

where $F_y = F_{yf} + F_{yr}$. Differentiating this constraint with respect to time prescribes $\dot{r}$ as a function of the lateral input $\dot{F}_y$. The required yaw moment and F_y uniquely determine the lateral forces at each axle, so the friction limitations of each axle can be considered individually. Since this is not a dynamic model, longitudinal load transfer is also assumed to remain in steady state. While the point-mass representation ignores a vehicle's yaw dynamics, combining it with friction circle constraints models the vehicle's acceleration for the purpose of trajectory planning.

G. State and Control Vectors for Each Model

Having introduced each model at a conceptual level, we can list the state and input vectors for each. The **double-track model** has state vector

$$ \vec{x}_{dt} = [u_y\ r\ u_x\ \Delta\psi\ e\ \Delta F_{z,\,long}\ \Delta F_{z,\,lat}\ \delta]^T \tag{32} $$

and its seven control inputs are contained in

$$ \vec{u}_{dt} = \Big[\dot{\delta}\ F_{xfl,\,brake}\ F_{xfr,\,brake}\ F_{xrl} $$

$$ \dots F_{xrr}\ F_{engine}\ u_{diff}\Big]^T \tag{33} $$

Since the vehicle considered here is front wheel drive, F_{xrl} and F_{xrr} do not require any additional subscript to show that it is the longitudinal force from the rear brakes. The **single-track model** requires fewer variables to describe its state:

$$ \vec{x}_{st} = \begin{bmatrix} u_y & r & u_x & \Delta\psi & e & \Delta F_{z,\,long} & \delta \end{bmatrix}^T. $$

and has four control inputs

$$ \vec{u}_{st} = \begin{bmatrix} \dot{\delta} & F_{xf,\,brake} & F_{xr} & F_{engine} \end{bmatrix}^T. $$

The **point-mass model** has the smallest state vector with

$$ \vec{x}_{pm} = \begin{bmatrix} u_x & \Delta\psi & e & F_y \end{bmatrix}^T $$

for which the simplified equations of motion are

$$ \dot{u}_x = \frac{F_{xf} + F_{xr} - F_{drag}}{m} - q u_z + g_x \tag{34} $$

$$ \dot{\Delta\psi} = \frac{F_y}{m u_x} + \frac{p u_z + g_y}{u_x} - \dot{s}k \tag{35} $$

$$ \dot{e} = u_x \sin \Delta\psi. \tag{36} $$

To match the other models as closely as possible, the control inputs are

$$ \vec{u}_{pm} = \begin{bmatrix} \dot{F}_y & F_{xf,\,brake} & F_{xr} & F_{engine} \end{bmatrix}^T. $$

In total, the double-track model has 15 state and input variables, the single-track model 11, and the point-mass model just 8.

III. OPTIMAL CONTROL FORMULATION

Minimization of lap time for a given circuit is used as the objective in the optimal control problem so that the vehicle will be forced to operate at its modeled limits. However, the cost function is slightly augmented through the addition of other terms that encode a desire to minimize wear on the test vehicle for a given lap time;

$$ J = \int_0^{t_{final}} 1 + f(x, u)\, dt \tag{37} $$

where $f(x, u)$ contains the components of the cost function other than time,

$$ f(x, u) = q P_{tire} + r_1 P_{brake} + r_2 \dot{\delta}^2 + r_3 u_{diff}. \tag{38} $$

P_{brake} and P_{tire} are the rates of energy dissipation in the brakes and tires through sliding friction and $q = 5 \times 10^{-8}$, $r_1 = 1 \times 10^{-7}$, $r_2 = 0.1$, and $r_3 = 5 \times 10^{-3}$. Total work done by the brakes and sliding tires is used as a rough approximation to wear through abrasion. These additional terms enforce a preference for a trajectory that uses less control effort and produces less wear for a given lap time.

We use the same change of independent variable widely used in the trajectory optimization literature to circumvent the problem of an *a priori* unknown final time. By using distance along the path, s, instead of time as the independent variable, total elapsed time can be minimized directly. The equations of motion and the objective function can be mapped into the new

domain using the chain rule. The objective function, as used, is given by

$$J = \int_0^{s_{max}} \frac{1 + f(x, u)}{\dot{s}} \, ds \qquad (39)$$

where s_{max} is the length of the nominal path. This formulation is exactly equivalent to that in (37), but is more numerically expedient.

A. Constraints

The constraints used in the problem were limited to those necessary to capture the physical limitations of the car and its actuators and to produce useful solutions. The lateral position, e is bounded by the distance to the track edges ensuring the optimal trajectory remains within the track limits. While not an active constraint in any of the examples presented here, the magnitudes of the steering angle and steering rate are limited to their physical maximum values. The differential engagement must be bounded between zero and one, and the brake forces must be upper bounded by zero. The engine power output is bounded by the engine's maximum and minimum power outputs:

$$P_{min} \le F_{x, \, eng}(u_x \cos \delta + (u_y + ar) \sin \delta) \le P_{max} \quad (40)$$

For each of the four tires, the longitudinal forces are bounded by the available friction:

$$-\mu F_z \cos \alpha \le F_x \le \mu F_z \qquad (41)$$

Finally, to ensure continuity over the circuit, all variables are constrained to be continuous at the start/finish of the lap.

B. Implementation

We elected to solve the optimal control problem sketched above by a direct numerical method. Both the cost function in (39) and the differential equations describing the vehicle dynamics are approximated numerically via trapezoidal integration. The resulting nonlinear optimization problem is solved with Ipopt [43]. The required first and second derivatives are computed using CasADi [44]. Reasonable scaling of the problem variables is required to achieve acceptable speed and reliability though no effort was made to perfect this scaling. An arbitrary nominal path with continuous heading and curvature is chosen to define the coordinate system. This path is also used to compute a rough initial guess for the optimal velocity of the vehicle [45]. Discretization points were chosen to be evenly spaced in time based on the initial guess for the speed profile.

IV. OPTIMIZATION RESULTS

In order to see how the choice of model affects the trajectory of the vehicle, we first compare the optimal trajectory for each model in a simple case, a small oval on dry asphalt. A comparison of the counter-clockwise paths is shown in Fig. 5. The trajectories are similar, but there are a few noticeable differences. The constrained double-track model has the tightest exit while entering the corner the farthest to the outside. The relative straightness of its path while exiting the corner is explained by the fact that it has the greatest difficulty accelerating and
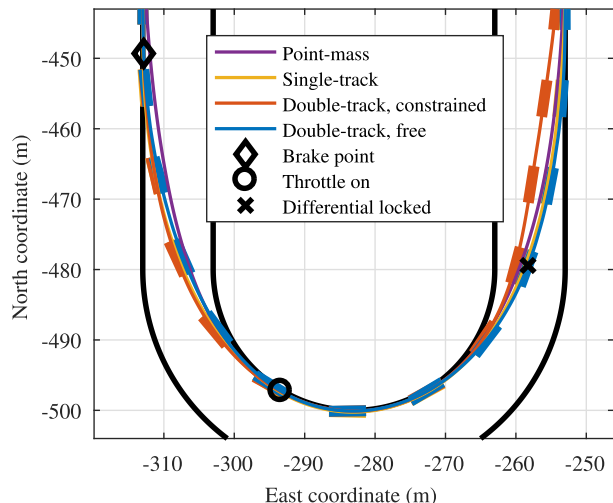
Fig. 5. Optimal path and vehicle orientation for each trajectory. The line segments showing the vehicle's orientation are twice the length of the vehicle's wheelbase.
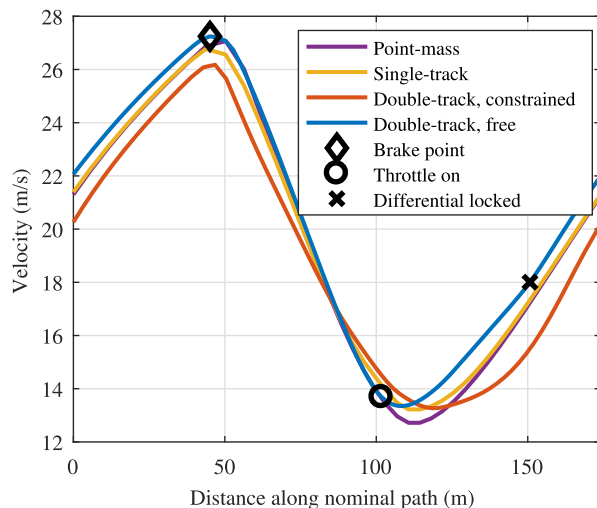
Fig. 6. Velocity profile for each trajectory.

cornering simultaneously. Since it lacks the ability to torque vector, the constrained double-track model is limited by the lightly loaded inner front wheel which forces the prioritization of acceleration over cornering. Conversely, the unconstrained double-track model takes the widest exit and is unique in that it maintains a nose-in attitude throughout the corner. The point-mass and single-track trajectories lie between the other two although the point-mass minimizes time spent cornering, taking a straighter entry and exit to the corner.

The differences in the velocity traces and lap times mirror those in the racing lines as shown in Fig. 6. The point-mass and single-track models are again similar though the point-mass has a lower minimum velocity. The unconstrained double-track model reaches its minimum speed earliest in the corner, has a relatively rapid transition from braking to acceleration, and shows the highest exit speed while the constrained version does
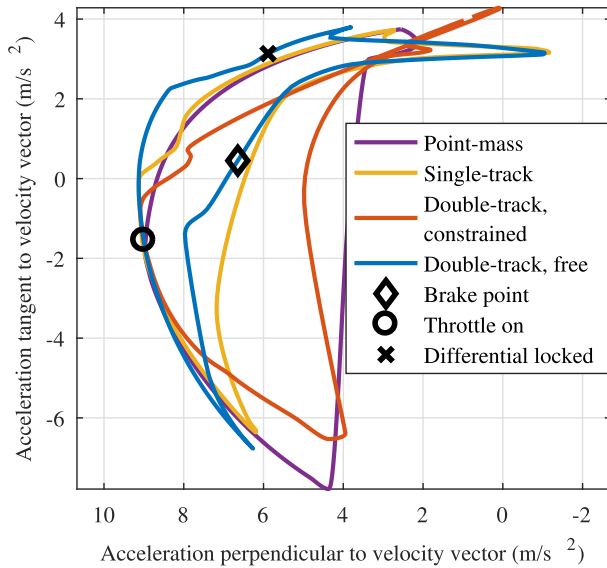
Fig. 7.   Acceleration achieved by each model.

exactly the opposite. The optimal lap times match the trends seen in the speed profiles. The unconstrained double-track model is fastest with a 17.45 s lap. The single-track and point-mass are comparable with a 17.90 and an 18.03, respectively, while the constrained double-track model is slowest with an 18.47.

Comparing the acceleration potentials of the models explains the differences seen in the optimal trajectories and lap times. Cornering and longitudinal accelerations for a single corner of the oval are shown in Fig. 7. Looking at the performance during combined deceleration and cornering, in the lower left part of the diagram, we see that the constrained double-track model has the most limited performance since this model must respect the friction limitations of each tire, not just each axle like the single-track and point-mass models. Therefore, it is limited by the less lightly loaded inner tire on each axle. By dividing the braking force across the axle, the unconstrained double-track model generates slightly more deceleration than the single-track and point-mass models, which perform similarly. In the middle part of the corner, as the car is still slowing, all the dynamic models perform comparably while the point-mass model is the most limited. By over-rotating the car slightly, and building extra rear slip angle, the dynamic models can make maximal use of the rear tires' force potential, while the point-mass model is forced to remain in steady state. Acceleration out of the corner looks similar to corner entry. The constrained double-track model is limited by the lack of load on the inside front wheel. The point-mass and single-track predict a similar level of capability while the unconstrained double-track model has the greatest potential for combined cornering and acceleration. By generating the majority of acceleration from the outside front wheel, first by braking the inside front one then by locking the differential, the car can more efficiently use the front tires and create a yawing moment which is balanced by extra lateral force from the rear tires. In conclusion, the optimal trajectory for each model favors operating the vehicle in a way that emphasizes its

Fig. 8.   Test vehicle negotiating a corner at Thunderhill Raceway.

relative strengths, and there is a significant advantage to being able to divide longitudinal forces across the four tires efficiently in this scenario as evidenced by the lap times.

V. Experimental Results

Despite the differences in the optimization results, it remains to be seen whether the performance differences can be realized on an actual vehicle. In this section, the advantages of higher fidelity models for trajectory generation are assessed by using optimal trajectories generated using each model as a desired trajectory for an autonomous vehicle. While all models are only approximations to the vehicle's true dynamics, improvement in the accuracy and fidelity of the model used for trajectory optimization should lead to reduced tracking error and more nearly optimal performance on the real car.

The suitability of each model for trajectory planning was evaluated across three different surfaces using an autonomous vehicle. The data from these tests are available at https://drive.google.com/drive/folders/12VguJc_51IJmI80tgHBhZKVPKalgwIen?usp=sharing?. Tests on dry and wet asphalt were performed at the Thunderhill West circuit in Willows, CA, using a 2019 Volkswagen GTI, shown in Fig. 8, configured to allow fully autonomous operation. A frozen lake in northern Europe and an identical vehicle, apart from exterior color, were used to conduct tests in icy conditions. Friction coefficients for this vehicle are approximately 0.90 on dry asphalt, 0.72 on wet asphalt, and 0.26 on ice. The vehicle's ESC system has been bypassed although an ABS system is still present. An OxTS RT4003 DGPS/IMU system and an external GPS base station provide measurements of the vehicle's position to within centimeters. Control of steering, throttle, individual brake pressures, and the differential is performed by a low-level control computer operating at 200 Hz and communicating with the vehicle via multiple CAN buses.

A. Experimental Design

For a given surface condition, optimal trajectories were generated with each model and were then evaluated as to how well they could be tracked by the car. Parameters were generated for each model by optimizing the fit of the model to a number of previously collected datasets of the vehicle operating at the limits of grip on that surface. Taking the longitudinal velocity as a given,
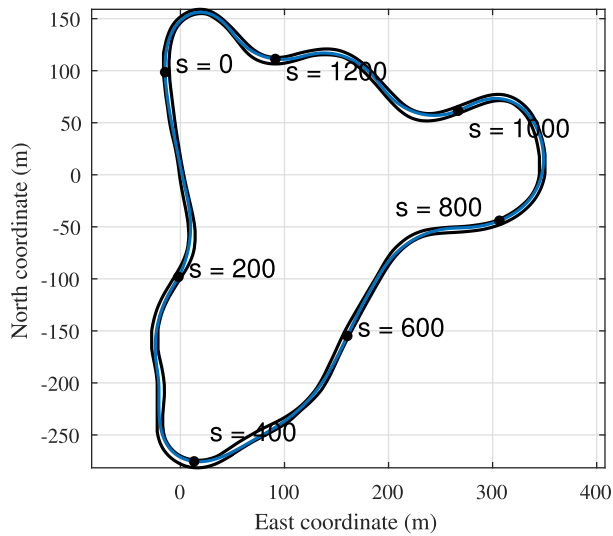
Fig. 9.   Blue curve shows the optimal path and the black curves mark the edges of the counter-clockwise handling track used for the experiments on ice.

Fig. 10.   Optimal speed profiles for the icy handling track generated with each model.

TABLE I
LAP TIME COMPARISON FOR RACING ON ICE

Model	Target Time (s)	Driven Time (s)	Deviation (s)
Point-mass	100.27	103.48	3.21
Single-track	101.14	102.61	1.47
Double-track, constrained	99.06	100.59	1.53
Double-track, free	98.02	98.69	0.68

open-loop prediction of the vehicle's lateral states served as an optimization criterion. This parameter optimization process was performed for the double-track and single-track models while the friction coefficients from the single-track model were used for the point-mass model. These parameters were then used to generate the optimal trajectories and feedforward control inputs for the car. The feedback steering controller from [46] and a longitudinal feedback law driven by deviation from the desired speed are used to compensate for disturbances and mismatch between the models and the actual vehicle.

B. Test Results on Ice

On the icy surface, load transfer is minimized, and the effects captured by the four wheel model are muted. The optimal path around the handling track for the unconstrained double-track model is plotted in Fig. 9. The paths for the other models are practically indistinguishable even when examined in detail. The optimal longitudinal velocities, shown in Fig. 10, also display little variation. This similarity is due to the fact that the additional control flexibility offered by the unconstrained double-track model is less advantageous in the absence of significant differences in the force potential between the two tires on an axle. In fact, the differential is not used at all by the unconstrained double-track model. Since one front tire never has enough grip to use even half of the engine's power output, there is no need to accept the additional constraint imposed by locking the differential. Instead, all torque vectoring is done with the brakes which creates a small improvement in mid-corner and exit speeds relative to the constrained double-track model.

This improvement in speed translates to a small improvement in lap time. The lap time of the nominal trajectory, the measured lap time, and the difference between them for the four trajectories are shown in Table I. Even in this limited case, the more complex models allow more performance to be extracted from the car. Later, we will see that the double-track models achieve closer speed tracking than the other two models which helps to reduce
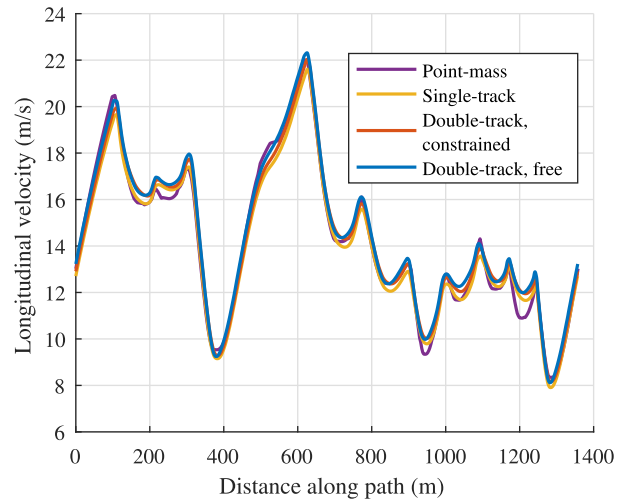
the discrepancy in lap time. One reason for this difference is that it is easy for the vehicle to break traction with the application of longitudinal force on such a slippery surface. The double-track models do a better job of limiting significant longitudinal wheel slip since they capture the friction limitations of each wheel. In this case, increasing model fidelity improves both the resulting lap time and the match to the target trajectory.

The experimental results from the tests on ice also revealed one reason to favor the more computationally expensive models over the point-mass; these models capture the transient yaw dynamics and the effect of longitudinal inputs on those dynamics. In contrast, the yaw dynamics are not particularly well controlled when negotiating transitions between corners with the trajectory generated with the point-mass model. Fig. 11 shows the vehicle states as the vehicle becomes unbalanced through the slight right hand corner before the longer left hand corner at the bottom of the map in Fig. 9. The vehicle is unbalanced by braking for the upcoming left hand corner while in the middle of the right hand corner. In the test, the vehicle adopts a high sideslip attitude before snapping back the other way. Once the vehicle takes a highly nose-in attitude to the left corner, the feedback controller is able to stabilize the vehicle and return it to steady state. This limitation was accentuated by the low friction and the many linked corners of the icy handling track. Similar behavior was not observed in the tests on wet and dry asphalt.

C. Test Results on Dry Asphalt

To illustrate the optimal coordination of the brakes and differential, we present data from the tests on dry asphalt. Conducted
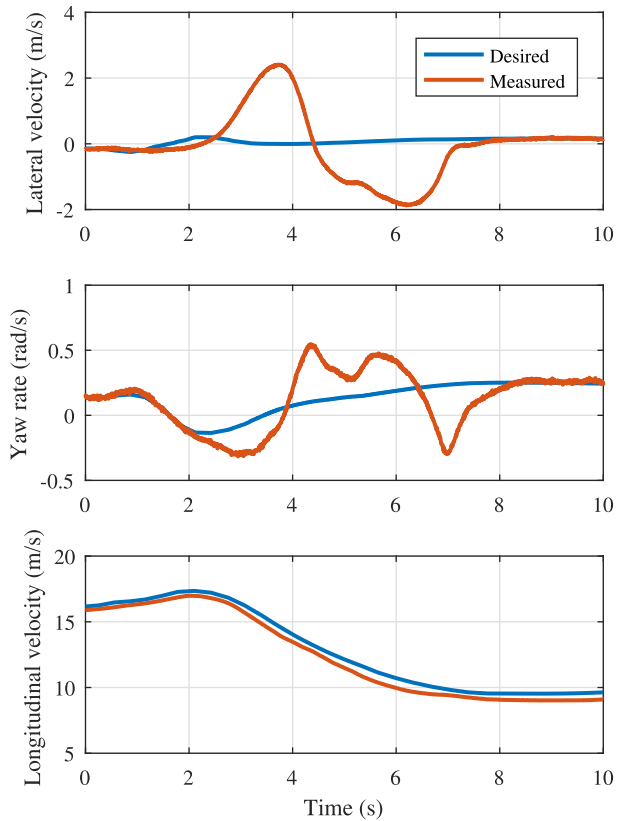
Fig. 11. Vehicle states during unintended pendulum maneuver while tracking the point-mass trajectory.
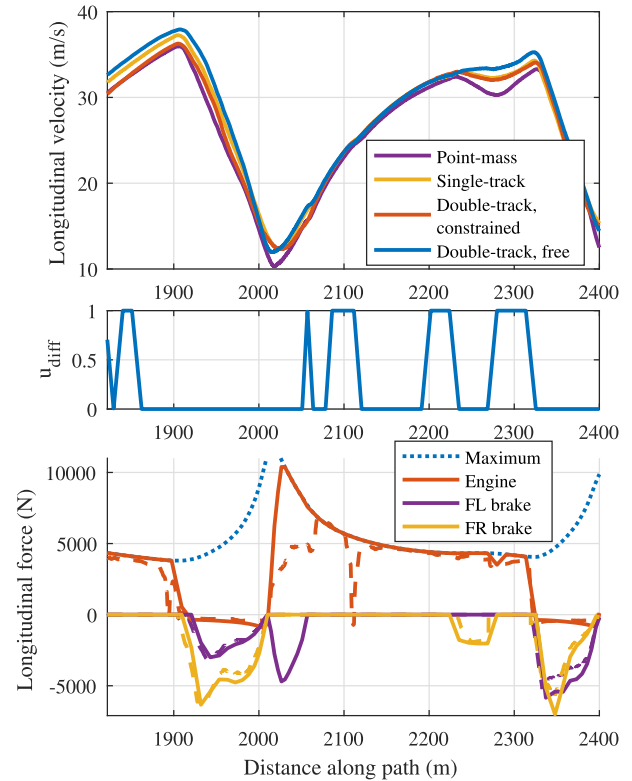

Fig. 12. Measured velocity for all trajectories and feedforward control inputs for the unconstrained double-track model (solid lines). The shortfall in estimated engine output is offset in the total brake commands (dashed lines).

over a portion of the Thunderhill West circuit, the tests consisted of the vehicle accelerating through the sweeping left hand Turn 6 then bending slightly to the right before braking hard for the tight left hand Turn 7. The vehicle reaches the friction limits in the right hand Turn 8 before braking immediately for Turn 9. The driven speed profiles from each model and the control inputs for the double-track model are shown in Fig. 12 beginning from the exit of Turn 6. Examining the velocity traces shows that the double-track model primarily gains an advantage in the faster corners. With the differential engaged, it is able to continue to fully accelerate through Turn 6 while the other models are forced to briefly reduce throttle resulting in a lower speed when approaching Turn 7. The differential is briefly disengaged before being reengaged for the slight right hand bend at 1840 meters along the path. For Turn 8, from 2190 to 2330 meters along the path, a combination of strategies are employed. The vehicle initially turns in at full throttle with the differential locked. In the middle of the corner, the differential is disengaged and the inside front brake is applied to limit the increase in vehicle speed, increase the normal load on the front tires, and create additional yawing moment. At the exit of the corner, the vehicle switches back to a locked differential initially with slightly reduced throttle to maximize speed before braking hard for Turn 9.

A comparison of section times between the various models is shown in Table II. Given the increased load transfer on dry asphalt, it would be reasonable to expect a larger advantage for

TABLE II
SECTION TIME COMPARISON FOR RACING ON DRY ASPHALT

Model	Target Time (s)	Driven Time (s)	Deviation (s)
Point-mass	22.85	24.17	1.32
Single-track	22.33	22.74	0.41
Double-track, constrained	22.84	23.28	0.44
Double-track, free	21.83	22.50	0.67

the double-track model than was observed. However, this effect is offset by the fact that the car is limited by engine power, not tire grip, for much of the segment in dry conditions. This is in stark contrast to driving on ice where the front tires are operating at the limits of adhesion over the entire lap. As a result, there are only a few places over the segment where the double-track model is able to capitalize on its more efficient use of the available friction.

D. Trends in Path and Speed Tracking Across Friction Values

The previous sections showed examples of where higher fidelity models and increased control flexibility could be expected to lead to better performance. However, this improvement comes from increasing the acceleration potential of the car rather than predicting the states more accurately. In this section, the path and speed tracking errors for the vehicle following the various optimal trajectories are compared to show that any of

TABLE III
SPEED TRACKING ROOT MEAN SQUARE ERROR ACROSS FRICTION CONDITIONS

Speed tracking RMSE (m/s)	Ice	Wet Asphalt	Dry Asphalt
Point-mass	0.48	0.53	1.28
Single-track	0.23	0.30	0.71
Double-track, constrained	0.22	0.34	0.67
Double-track, free	0.15	0.25	0.87

TABLE IV
PATH TRACKING ROOT MEAN SQUARE ERROR ACROSS FRICTION CONDITIONS

Lateral error, e (m)	Ice	Wet Asphalt	Dry Asphalt
Point-mass	0.31	0.25	0.20
Single-track	0.24	0.45	0.28
Double-track, constrained	0.18	0.3	0.20
Double-track, free	0.26	0.33	0.29

the models can be used to generate feasible trajectories for a vehicle. Table III shows that the point-mass model has the worst speed tracking and that RMSE was observed to increase with friction coefficient. The tracking error for the point-mass is higher in general since the model does not directly account for the drag produced by cornering. Note also that the tracking error increases along with the friction coefficient since on higher traction surfaces producing maximum torque and ensuring the transmission is in the correct gear becomes more critical.

While the more complex models produce a closer match of speed, the point-mass model actually demonstrates the most accurate path tracking in the majority of cases as shown in Table IV. The one exception to the trend is the data from the icy conditions where it produces the worst. This pattern is explained by the following observation. Despite not capturing the yaw dynamics of the vehicle, accurate feedforward slip angles can be produced for the point-mass model trajectory assuming a steady-state cornering condition. This works well so long as the car remains near steady-state, but when the car over rotates while transitioning between corners there is significant tracking error as the steering controller stabilizes the vehicle.

VI. CONCLUSION

The selection of a model for optimal control represents a trade-off between simplicity and the level of nuance in the model's prediction of the vehicle's limits. The model used does not have a major effect on the optimal path or speed for the vehicle. Even a point-mass model is sufficient in this respect. However, the point-mass model fails to capture transient dynamics which can be critical on low friction surfaces though tracking under steady state conditions can be excellent. In contrast, the single-track model better captures transient dynamics, particularly when transitioning between corners at nearly constant speed. Finally, the double-track model is most valuable for modeling the vehicle's limits when considering aggressive combined lateral and longitudinal acceleration. While the most computationally expensive, a double-track model allows the effects of differential braking and a controllable LSD to be captured. By leveraging control of the differential and the individual brakes, the car can enter a corner faster, mitigate understeer in the middle and latter

TABLE V
VEHICLE PARAMETERS

Symbol	Description	Value
a	Distance from c.g. to front axle	1.19 m
b	Distance from c.g. to rear axle	1.44 m
d_f	Front track width	1.54 m
d_r	Rear track width	1.52 m
h_{cg}	Center of gravity height	0.56 m
γ	Front lateral load transfer fraction	0.64
m	Vehicle mass	1776 kg
I_{xx}	Moment of inertia about longitudinal axis	1200 kgm^2
I_{yy}	Moment of inertia about lateral axis	3200 kgm^2
I_{zz}	Moment of inertia about vertical axis	3950 kgm^2
K_{lat}	Lateral load transfer time constant	23.2 s^{-1}
K_{long}	Longitudinal load transfer time constant	15.7 s^{-1}

TABLE VI
TIRE PARAMETERS FOR ICE

	Double-track	
Symbol	Description	Value
F_{z0}	Nominal normal load	4470 N
μ_0	Nominal friction coefficient	0.267
μ_{df_z}	Friction sensitivity	-0.011
c_1	Lateral stiffness parameter	22.0
c_2	Lateral stiffness peak	2.14
n	Lateral-longitudinal coupling	4.23
c_8	Longitudinal stiffness	10
	Single-track and Point-mass	
Symbol	Description	Value
μ_f	Front friction coefficient	0.251
μ_r	Rear friction coefficient	0.256
$C_{\alpha,\,f}$	Front cornering stiffness	1.38e5 N
$C_{\alpha,\,r}$	Rear cornering stiffness	1.39e5 N
n_f	Front lateral-longitudinal coupling	3.0
n_r	Rear lateral-longitudinal coupling	4.1

TABLE VII
TIRE PARAMETERS FOR WET ASPHALT

	Double-track	
Symbol	Description	Value
F_{z0}	Nominal normal load	4470 N
μ_0	Nominal friction coefficient	0.81
μ_{df_z}	Friction sensitivity	-0.232
c_1	Lateral stiffness parameter	22.8
c_2	Lateral stiffness peak	1.5
n	Lateral-longitudinal coupling	2.5
c_8	Longitudinal stiffness	6.55
	Single-track and Point-mass	
Symbol	Description	Value
μ_f	Front friction coefficient	0.721
μ_r	Rear friction coefficient	0.90
$C_{\alpha,\,f}$	Front cornering stiffness	2.4e5 N
$C_{\alpha,\,r}$	Rear cornering stiffness	3.0e5 N
n_f	Front lateral-longitudinal coupling	2.1
n_r	Rear lateral-longitudinal coupling	3.7

parts of the corner, and increase exit speed. The experiments in this paper suggest that the expected improvements can be realized in the real world.

APPENDIX

The vehicle parameters for the three surface conditions are collected in Tables V–VIII.

TABLE VIII
TIRE PARAMETERS FOR DRY ASPHALT

Double-track		
Symbol	Description	Value
F_{z0}	Nominal normal load	8940 N
μ_0	Nominal friction coefficient	0.90
μ_{df_z}	Friction sensitivity	-0.13
c_1	Lateral stiffness parameter	17.0
c_2	Lateral stiffness peak	1.14
n	Lateral-longitudinal coupling	4.03
c_8	Longitudinal stiffness	12.8
Single-track and Point-mass		
Symbol	Description	Value
μ_f	Front friction coefficient	0.873
μ_r	Rear friction coefficient	1.03
$C_{\alpha,\,f}$	Front cornering stiffness	1.76e5 N
$C_{\alpha,\,r}$	Rear cornering stiffness	2.26e5 N
n_f	Front lateral-longitudinal coupling	8.0
n_r	Rear lateral-longitudinal coupling	3.0

ACKNOWLEDGMENT

REFERENCES

[1] R. S. Sharp and H. Peng, "Vehicle dynamics applications of optimal control theory," *Veh. Syst. Dyn.*, vol. 49, no. 7, pp. 1073–1111, 2011.

[2] K. Liu, J. Gong, A. Kurt, H. Chen, and U. Ozguner, "Dynamic modeling and control of high-speed automated vehicles for lane change maneuver," *IEEE Trans. Intell. Veh.*, vol. 3, no. 3, pp. 329–339, Sep. 2018.

[3] B. Gutjahr, L. Gröll, and M. Werling, "Lateral vehicle trajectory optimization using constrained linear time-varying MPC," *IEEE Trans. Intell. Transp. Syst.*, vol. 18, no. 6, pp. 1586–1595, Jun. 2017.

[4] J. Funke, M. Brown, S. M. Erlien, and J. C. Gerdes, "Collision avoidance and stabilization for autonomous vehicles in emergency scenarios," *IEEE Trans. Control Syst. Technol.*, vol. 25, no. 4, pp. 1204–1216, Jul. 2017.

[5] A. Liniger, A. Domahidi, and M. Morari, "Optimization-based autonomous racing of 1 : 43 scale RC cars," *Optimal Control Appl. Methods*, vol. 36, no. 5, pp. 628–647, 2015.

[6] G. Prokop, "Modeling human vehicle driving by model predictive online optimization," *Veh. Syst. Dyn.*, vol. 35, no. 1, pp. 19–53, 2001.

[7] P. A. Theodosis and J. C. Gerdes, "Nonlinear optimization of a racing line for an autonomous racecar using professional driving techniques," in *Proc. ASME 2012 5th Annu. Dynamic Systems Control Conf.*, 2012, pp. 235–241, doi: 10.1115/DSCC2012-MOVIC2012-8620.

[8] N. R. Kapania, J. Subosits, and J. C. Gerdes, "A sequential two-step algorithm for fast generation of vehicle racing trajectories," *J. Dyn. Syst., Meas., Control*, vol. 138, no. 9, 2016, Art. no. 091005.

[9] P. Falcone, F. Borrelli, H. E. Tseng, J. Asgari, and D. Hrovat, "A hierarchical model predictive control framework for autonomous ground vehicles," in *Proc. Amer. Control Conf.*, 2008, pp. 3719–3724.

[10] J. Ziegler, P. Bender, T. Dang, and C. Stiller, "Trajectory planning for bertha—A local, continuous method," in *Proc. Intell. Veh. Symp.*, 2014, pp. 450–457.

[11] F. Altché, P. Polack, and A. de La Fortelle, "High-speed trajectory planning for autonomous vehicles using a simple dynamic model, in intelligent transportation systems (ITSC), in *Proc. IEEE 20th Int. Conf.*, 2017, pp. 1–7.

[12] J. K. Subosits and J. C. Gerdes, "From the racetrack to the road: Real-time trajectory replanning for autonomous driving," *IEEE Trans. Intell. Veh.*, vol. 4, no. 2, pp. 309–320, Jun. 2019.

[13] J. P. Timings and D. J. Cole, "Minimum maneuver time calculation using convex optimization," *J. Dyn. Syst., Meas., Control*, vol. 135, no. 3, 2013, Art. no. 031015.

[14] E. Velenis and P. Tsiotras, "Minimum time vs maximum exit velocity path optimization during cornering," in *Proc. IEEE Int. Symp. Ind. Electron.*, 2005, pp. 355–360.

[15] B. Olofsson, K. Lundahl, K. Berntorp, and L. Nielsen, "An investigation of optimal vehicle maneuvers for different road conditions," *IFAC Proc. Vol.*, vol. 46, no. 21, pp. 66–71, 2013.

[16] D. Tavernini, M. Massaro, E. Velenis, D. I. Katzourakis, and R. Lot, "Minimum time cornering: The effect of road surface and car transmission layout," *Veh. Syst. Dyn.*, vol. 51, no. 10, pp. 1533–1547, 2013.

[17] A. Rucco, G. Notarstefano, and J. Hauser, "Computing minimum lap-time trajectories for a single-track car with load transfer," in *Proc. IEEE 51st IEEE Conf. Decis. Control*, 2012, pp. 6321–6326.

[18] M. Brown, J. Funke, S. Erlien, and J. C. Gerdes, "Safe driving envelopes for path tracking in autonomous vehicles," *Control Eng. Pract.*, vol. 61, pp. 307–316, 2017.

[19] D. P. Kelly and R. S. Sharp, "Time-optimal control of the race car: A numerical method to emulate the ideal driver," *Veh. Syst. Dyn.*, vol. 48, no. 12, pp. 1461–1474, 2010.

[20] G. Perantoni and D. J. N. Limebeer, "Optimal control for a formula one car with variable parameters," *Veh. Syst. Dyn.*, vol. 52, no. 5, pp. 653–678, 2014.

[21] N. Dal Bianco, E. Bertolazzi, F. Biral, and M. Massaro, "Comparison of direct and indirect methods for minimum lap time optimal control problems," *Veh. Syst. Dyn.*, vol. 57, no. 5, pp. 665–696, 2019.

[22] K. Berntorp, B. Olofsson, K. Lundahl, and L. Nielsen, "Models and methodology for optimal trajectory generation in safety-critical road-vehicle manoeuvres," *Veh. Syst. Dyn.*, vol. 52, no. 10, pp. 1304–1332, 2014.

[23] F. Gottmann, H. Wind, and O. Sawodny, "On the influence of rear Axle steering and modeling depth on a model based racing line generation for autonomous racing," in *Proc. IEEE Conf. Control Technol. Appl.*, 2018, pp. 846–852.

[24] J. Liu, P. Jayakumar, J. L. Stein, and T. Ersal, "A study on model fidelity for model predictive control-based obstacle avoidance in high-speed autonomous ground vehicles," *Veh. Syst. Dyn.*, vol. 54, no. 11, pp. 1629–1650, 2016.

[25] S. M. Laws, C. D. Gadda, and J. C. Gerdes, "Frequency characteristics of vehicle handling: Modeling and experimental validation of yaw, sideslip, and roll modes to 8hz," in *Proc. Int. Symp. Adv. Veh. Control*, Taipei, Taiwan, 2006, pp. 901–906.

[26] J. Kim, "Effect of vehicle model on the estimation of lateral vehicle dynamics," *Int. J. Automot. Technol.*, vol. 11, no. 3, pp. 331–337, 2010.

[27] K. U. Henning and O. Sawodny, "Vehicle dynamics modelling and validation for online applications and controller synthesis," *Mechatronics*, vol. 39, pp. 113–126, 2016.

[28] E. K. Liebemann, K. Meder, J. Schuh, and G. Nenninger, "Safety and performance enhancement: The bosch electronic stability control (ESP)," *SAE Paper*, vol. 2004, pp. 21–60, 2004.

[29] A. Lutz, J. Rauh, and W. Reinalter, "Developments in vehicle dynamics and the tire model performance test," *Veh. Syst. Dyn.*, vol. 45, no. suppl. 1, pp. 7–19, 2007.

[30] S. A. Ferguson, "The effectiveness of electronic stability control in reducing real-world crashes: A literature review," *Traffic Injury Prevention*, vol. 8, no. 4, pp. 329–338, 2007.

[31] K. Sawase, Y. Ushiroda, and K. Inoue, "Effect of the right-and-left torque vectoring system in various types of drivetrain," *SAE Tech. Paper Ser.*, vol. 1, no. 724, 2010, doi: 10.4271/2007-01-3645.

[32] M. Jonasson, J. Andreasson, B. Jacobson, and A. S. Trigell, "Global force potential of over-actuated vehicles," *Veh. Syst. Dyn.*, vol. 48, no. 9, pp. 983–998, 2010.

[33] R. De Castro, M. Tanelli, R. E. Araújo, and S. M. Savaresi, "Minimum-time manoeuvring in electric vehicles with four wheel-individual-motors," *Veh. Syst. Dyn.*, vol. 52, no. 6, pp. 824–846, 2014.

[34] E. N. Smith, E. Velenis, D. Tavernini, and D. Cao, "Effect of handling characteristics on minimum time cornering with torque vectoring," *Veh. Syst. Dyn.*, vol. 56, no. 2, pp. 221–248, 2018.

[35] M. J. Hancock, R. A. Williams, E. Fina, and M. C. Best, "Yaw motion control via active differentials," *Trans. Inst. Meas. Control*, vol. 29, no. 2, pp. 137–157, 2007.

[36] D. J. N. Limebeer and G. Perantoni, "Optimal control of a formula one car on a three-dimensional track-Part 2: Optimal control," *J. Dyn. Syst., Meas., Control*, vol. 137, no. 5, 2014, Art. no. 051019.

[37] A. J. Tremlett, F. Assadian, D. J. Purdy, N. Vaughan, A. P. Moore, and M. Halley, "Quasi-steady-state linearisation of the racing vehicle acceleration envelope: A limited slip differential example," *Veh. Syst. Dyn.*, vol. 52, no. 11, pp. 1416–1442, 2014.

[38] A. J. Tremlett *et al.*, "Optimal control of motorsport differentials," *Veh. Syst. Dyn.*, vol. 53, no. 12, pp. 1772–1794, 2015.

[39] W. R. Garrott, "Measured vehicle inertial parameters-NHTSA's data through September 1992," SAE Tech. Paper, Tech. Rep. 930897, 1993.

[40] E. Fiala, "Lateral forces on rolling pneumatic tires," *V.D.I. Zeitschrift*, in German, vol. 96, no. 29, pp. 973–979, 1954.

[41] H. Pacejka, *Tire and Vehicle Dynamics*. Burlington, MA, USA: Butterworth-Heinemann, 2005.

[42] P. Haney, *Racing & High-Performance Tire: Using the Tires to Tune for Grip and Balance*. Warrendale, PA, USA: SAE, 2003.

[43] A. Wächter and L. T. Biegler, "On the implementation of an interior-point filter line-search algorithm for large-scale nonlinear programming," *Math. Comput.*, vol. 106, no. 1, pp. 25–57, 2006.

[44] J. A. E. Andersson, J. Gillis, G. Horn, J. B. Rawlings, and M. Diehl, "CasADi—A software framework for nonlinear optimization and optimal control," *Math. Program. Comput.*, vol. 11, pp. 1–36, 2019.

[45] J. Subosits and J. C. Gerdes, "Autonomous vehicle control for emergency maneuvers: The effect of topography," in *Proc. Amer. Control Conf.*, 2015, pp. 1405–1410.

[46] N. R. Kapania and J. C. Gerdes, "Design of a feedback-feedforward steering controller for accurate path tracking and stability at the limits of handling," *Veh. Syst. Dyn.*, vol. 3114, pp. 1687–1704, 2015.

John K. Subosits received the B.S.E. degree in mechanical and aerospace engineering from Princeton University, Princeton, NJ, USA, in 2013 and the Ph.D. degree in mechanical engineering from Stanford University, Stanford, CA, USA, in 2020. His research interests include optimal control and trajectory planning for vehicles operating at the limits of handling.

J. Christian Gerdes received the Ph.D. degree from the University of California at Berkeley, Berkeley, CA, USA, in 1996. He is currently a Professor in mechanical engineering with Stanford University, Stanford, CA, USA, and the Director of the Center for Automotive Research with Stanford, Stanford University. His laboratory studies how cars move, how humans drive cars, and how to design future cars that work cooperatively with the driver or drive themselves. When not teaching on campus, he can often be found at the racetrack with students trying out their latest prototypes for the future.